**RESEARCH ARTICLE**

# Evaluation of boundary layer cloud parameterizations in the ECHAM5 general circulation model using CALIPSO and CloudSat satellite data

**Christine C. W. Nam[1,2], Johannes Quaas[1,2], Roel Neggers[3], Colombe Siegenthaler-Le Drian[4], and Francesco Isotta[4,5]**

[1]Max Planck Institute for Meteorology, Hamburg, Germany, [2]Leipzig Institute for Meteorology, Universität Leipzig, Leipzig, Germany, [3]Faculty of Mathematics and Natural Sciences, University of Cologne, Cologne, Germany, [4]Swiss Federal Institute of Technology (ETHZ), Zurich, Switzerland, [5]Now at MeteoSwiss, Zurich, Switzerland

**Abstract** Three different boundary layer cloud models are incorporated into the ECHAM5 general circulation model (GCM) and compared to CloudSat and CALIPSO satellite observations. The first boundary layer model builds upon the standard Tiedtke (1989) parameterization for shallow convection with an adapted convective trigger; the second is a bulk parameterization of the effects of transient shallow cumulus clouds; and lastly the Dual Mass Flux (DMF) scheme adjusted to better represent shallow convection. The three schemes improved (Sub)Tropical oceanic low-level cloud cover, however, the fraction of low-level cloud cover remains underestimated compared to CALIPSO observations. The representation of precipitation was improved by all schemes as they reduced the frequency of light intensity events $<0.01$ mm d$^{-1}$, which were found to dominate the radar reflectivity histograms as well as be the greatest source of differences between ECHAM5 and CloudSat radar reflectivity histograms. For both lidar and radar diagnostics, the differences amongst the schemes are smaller than the differences compared to observations. While the DMF approach remains experimental, as its top-of-atmosphere radiative balance has not been retuned, it shows the most promise in producing nonprecipitating boundary layer clouds. With its internally consistent boundary layer scheme that uses the same bimodal joint distribution with a diffusive and an updraft component for clouds and turbulent transport, the ECHAM5_DMF produces the most realistic boundary layer depth as indicated by the cloud field. In addition, it reduced the frequency of large-scale precipitation intensities of $<0.01$ mm d$^{-1}$ the greatest.

## 1. Introduction

The spread in climate sensitivity amongst General Circulation Models (GCMs) is dominated by cloud-climate feedbacks [*Cess et al.*, 1990; *Soden and Held*, 2006; *Ringer et al.*, 2006]; low-level clouds contribute the most to these differences in the tropics [*Vial et al.*, 2013; *Bony and Dufresne*, 2005]. Understanding how boundary layer clouds, those within the lowest 3–4 km of the Earth's atmosphere, change in a perturbed climate is vital to the cloud-climate feedback problem.

Boundary layer clouds are directly affected by the surface topography and surface fluxes. Their extent is largely determined by turbulence and inversion strength. The turbulent kinetic energy is related to the coupling of various processes in the boundary layer, such as cloud top entrainment and radiative cooling, neither of which are properly represented in a GCM. The coarse vertical resolution of GCMs and the inability of the advection scheme to capture sharp gradients make modeling the inversion difficult in GCMs. Since neither the turbulent kinetic energy nor inversion stability is modeled well, GCMs in general have difficulties to realistically represent boundary layer clouds.

Low-level clouds in European Centre/Hamburg (ECHAM5) are poorly represented compared to CALIPSO and CloudSat satellite retrievals [*Nam and Quaas*, 2012] motivating the study of different boundary layer cloud parameterizations which apply various approaches for the representation of turbulent kinetic energy and inversion stability. This paper compares three new parameterization schemes to the standard ECHAM5 convective mass flux scheme (referred to as ECHAM5_Std) [*Tiedtke*, 1989]. These schemes include: (i) a modified version of the *Tiedtke* [1989] scheme in which a new convective trigger is employed (referred to as

ECHAM5_Trig; E. Roeckner and M. Esch, Modifications to the trigger of cumulus convection in ECHAM5, Max Planck Institute for Meteorology, Hamburg, Germany, personal communication, 2010); (ii) a bulk parameterization of the effects of transient shallow cumulus clouds (referred to as ECHAM5_VSMF) [*Von Salzen and McFarlane*, 2002; *Isotta et al.*, 2011]; and (iii) a Dual Mass Flux (DMF) scheme adjusted to better represent shallow convection (referred to as ECHAM5_DMF) [*Neggers et al.*, 2009]. These are changes primarily to the parameterization of shallow convection. The aim of this paper is to determine whether different representations of boundary layer clouds in the ECHAM5 GCM improve the representation of present-day cloud and precipitation distributions.

If a scheme captures the boundary layer clouds and the transitions between different cloud-types well, it indicates the vertical turbulence fluxes of heat, moisture, and momentum and their relationship to cloud cover have been successfully modeled [*Siebesma et al.*, 2003; *Svensson et al.*, 2000; *Karlsson et al.*, 2008]. If different boundary layer cloud regimes, which have vastly different radiative effects, are poorly reproduced by models in present-day simulations, it is unlikely these models will show much skill in reproducing cloud regime-type feedbacks [*Webb et al.*, 2001]. In order to evaluate how well these parameterizations represent the stratocumulus and shallow cumulus clouds, the modeled clouds will be evaluated against satellite observations from CALIPSO and CloudSat. The active instruments onboard these two satellites allow the vertical distribution of clouds and precipitation of the four boundary layer parameterizations to be evaluated. To compare the modeled clouds with those found in observations, the lidar and radar satellite simulators within the Cloud Feedback Model Intercomparison Project Observational Simulator Package (COSP) are used [*Bodas-Salcedo et al.*, 2011].

This paper is organized such that the CALIPSO and CloudSat satellites, their data sets, and their simulators are introduced in section 2. A description of the ECHAM5 model, boundary layer parameterizations, and experimental setup follows in section 3. The results are shown as evaluation against the CALIPSO lidar observations focusing on cloud abundance in section 4, and against CloudSat radar observations focusing on hydrometeor (cloud plus precipitation) characteristics in sections 5 and 6. Conclusions are presented in section 7.

## 2. Satellites and Simulators

The CALIPSO and CloudSat satellites are part of the A-Train constellation of sun-synchronous polar orbiting satellites 705 km above the sea surface. With a 98.2° inclination, they cover 82°S to 82°N and have a 16 day repeat cycle [*Winker et al.*, 2007]. The ascending limb crosses the equator at approximately 13:30 h, local solar time. The following sections provide a brief description of the lidar and radar instruments onboard of CALIPSO and CloudSat, respectively, as well as the CLIMSERV satellite data sets used in this study.

### 2.1. CALIPSO
The CALIPSO satellite hosts the Cloud-Aerosol Lidar with Orthogonal Polarization (CALIOP) instrument; a near-nadir 1064 and 532 nm wavelength lidar that provides global high-resolution profiles of the vertical structure of clouds and aerosols [*Winker et al.*, 2007]. In this study, the measured scattering ratio of light scattered by atmospheric cloud particles to gas molecules from the GCM-Oriented CALIPSO Cloud Product (GOCCP) observational data set is used. The GOCCP data set, hereafter referred to as CALIPSO data, is derived from CALIOP Level 1B NASA Langley Atmospheric Sciences Data Center CALIPSO data sets. The instantaneous lidar Scattering Ratios (SR) are averaged onto a 40 Level, $2° \times 2°$ grid [*Chepfer et al.*, 2008].

### 2.2. CloudSat
CloudSat hosts a 94 GHz, near-nadir cloud radar instrument, provides a vertical profile of clouds and precipitation. Following *Marchand et al.* [2009], cloud and precipitation particles are henceforth collectively referred to as hydrometeors. Hydrometeor reflectivities from the CloudSat Geometric Profile data set 2B-GeoProf are the basis of the CloudSat satellite data used. Due to the short 3.3 mm wavelength, a minimum reflectivity of $-30$ dBZe threshold is defined because the radar reflectivities can be dominated by multiple scattering by hydrometeors or become fully attenuated [*Mace et al.*, 2007; *Marchand et al.*, 2008]. Additionally, the lowest 1 km of reflectivities are discarded due to ground clutter following *Tanelli et al.* [2008].

### 2.3. Satellite Simulators

The COSP CALIPSO lidar simulator (ACTSIM) [*Chepfer et al.*, 2008] and CloudSat radar simulator (QuickBeam) [*Haynes et al.*, 2007] are used in this study. The satellite simulators divide the following profiles of each atmospheric column into 50 subcolumns: temperature, pressure, cloud water content, cloud particle concentration, cloud fraction, as well as the flux of large-scale and convective precipitation, which includes rain and snow. Variability among the subcolums is generated by accounting for ECHAM5's maximum-random cloud-overlap assumption; where clouds in adjacent layers overlap maximally while groups of clouds separated by one or more clear layers are randomly overlapped. The cloud fraction (in case of the radar simulator hydrometeor fraction; referring to clouds and precipitation) of each subcolumn is assumed to be entirely cloudy (one) or noncloudy (zero), with the average over the subcolumns equaling the grid-box hydrometeor (cloud) fraction [*Klein and Jakob*, 1999; *Chepfer et al.*, 2008]. The liquid and ice water content is divided equally over the cloudy subcolumns, assuming a constant in-cloud water/ice content distribution over all subcolumns [*Klein and Jakob*, 1999]. The optical properties of the clouds are derived and the lidar scattering ratio and radar reflectivities are computed. By accounting for instrument sensitivity and using a common definition of cloud fraction (i.e., from the lidar simulator SR > 5 are denoted as clouds), satellite simulators provide a consistent manner of comparison between clouds simulated by climate models and satellite observations [*Chepfer et al.*, 2008, 2010]. Projected total cloud cover is obtained by the ratio of subcolumns identified as cloudy by the satellite simulators and the total number of subcolumns in which a valid satellite retrieval is simulated.

## 3. Model and Experiment Description

The ECHAM5 experiments presented in this paper have been run with COSP version 1.2.1 online for the year 2007 after a spin-up of 3 months from observationally prescribed sea surface temperature and sea ice extent distributions from the Atmospheric Model Intercomparison Project (AMIP2). Data were output at a three hourly interval. A comparison of June-July-August (JJA) 2007 with December-January-February (DJF) 2007 in the control experiment showed no significant difference in terms of the main results and conclusions of this study (not shown); therefore, the results presented in this paper are for the JJA 2007 period. The JJA period was determined to be an adequate duration to determine model performance and to identify model deficiencies by *Nam and Quaas* [2012].

The simulations have a resolution of a spectral transform triangular truncation at wave number 63 (T63), corresponding to 1.8° × 1.8° (~200 km × ~200 km), with 31 vertical levels (denoted as L31). Prognostic equations for temperature, vorticity, divergence, logarithm of surface pressure, as well as the mass mixing ratios of water vapor and cloud liquid, and ice water are solved. These equations are described in *Roeckner et al.* [2003].

### 3.1. Clouds in ECHAM5

In the standard ECHAM5 model (ECHAM5_Std), clouds and their properties are divided between stratiform and convective clouds, of which only the stratiform interact with radiation, while both types produce precipitation and release latent heat of phase transitions. The clouds are parameterized based upon the prognostic grid-mean variables of water vapor, temperature, cloud liquid water and cloud ice; all of which are transported using a flux form semi-Lagrangian transport scheme [*Lin and Rood*, 1996].

Convection is triggered when air parcels lifted dry adiabatically to the lifting condensation level are positively buoyant with respect to their surroundings. Convection in ECHAM5 is founded on the *Tiedtke* [1989] mass flux concept and bulk cloud model. The mass flux is determined by the mass of air entrained and detrained from the convective plume. Entrainment and detrainment are separated into two categories: those which occur at the top of rising clouds and those which occur at the sides of clouds, below the rising top. The entrainment and detrainment rates are dependent on whether convection is classified as penetrative, midlevel or shallow. *Tiedtke* [1989] assumed the entrainment and detrainment rates to be $1 \times 10^{-4}$ $m^{-1}$ for penetrative deep convection and $3 \times 10^{-4}$ $m^{-1}$ for shallow convection. The fixed fractional entrainment and detrainment rates are an order of magnitude smaller [*Siebesma and Cuijpers*, 1995; *Wang et al.*, 2007] in order to permit convection to penetrate to high altitudes causing the shallow convection mass flux to be overestimated [*Isotta et al.*, 2011]. As such, the representation of penetrative convection, which occurs when large-scale convergence of moisture into the column is greater than the surface

evaporation, includes three key modifications by *Nordeng* [1994]. These include making organized entrainment as a function the updraft buoyancy, organized detrainment as scaling with height beginning from the "lowest level of organized detrainment possible," and lastly, defining the cloud base mass flux using a quasiequilibrium for convective instability [*Moebis and Stevens*, 2012]. Midlevel convection initiates above the boundary layer and forms when large-scale convergence at low levels is inhibited by a temperature inversion. Shallow convection occurs when the surface evaporation is larger than the large-scale convergence; and is mainly influenced by the turbulent surface moisture flux in the boundary layer. The convective cloud fraction is assumed negligible in ECHAM5; however, the water detrained from convective updrafts is treated as a source to the stratiform cloud cover scheme, contributing to the stratiform cloud cover in a grid box [*Lohmann and Roeckner*, 1996].

The mass mixing ratios of water vapor, cloud liquid water, and cloud ice are prognostically calculated using the bulk cloud microphysics scheme of *Lohmann and Roeckner* [1996]. The cloud fraction of a grid box is determined by integrating over the saturated part of the subgrid-scale total water mixing ratio probability density function (PDF) [*Tompkins*, 2002]; whose shape is defined by the prognostic variance and skewness parameters. The parameters are related to subgrid scale turbulence and convection; with a wider PDF indicative of a wide range of total water mixing ratios and a positively skewed PDF indicative of areas with concentrated water contents.

The cloud cover of a column, i.e., area covered by clouds if one looked down upon a column of atmospheric grid boxes, is determined assuming a maximum-random overlap.

### 3.2. Convective Mass Flux With Modified Convective Trigger

The ECHAM5_Trig model includes a modified version of the convection scheme in ECHAM5_Std. In the standard version of ECHAM5, convection occurs if surface air, lifted dry-adiabatically to the lifting condensation level, is found to be more buoyant than the environmental air. The buoyancy of the surface air parcel is defined as the difference in virtual temperature between the parcel and the environment. To account to some degree for subgrid variability, a constant of 0.5 K is added to the virtual temperature of the parcel. This adjustment is referred to as the convective trigger. In the ECHAM5_Trig, the convective trigger is modified such that the constant 0.5 K is replaced with more physical value, the standard deviation of the virtual potential temperature [*Stevens et al.*, 2013; E. Roeckner and M. Esch, personal communication, 2010]. This term is calculated at the lifting condensation level in the same manner as the vertical diffusion of heat and moisture and then applied to all subcloud layers. Lower and upper thresholds, 0.025 and 1.0, respectively, have been applied to the standard deviation of virtual potential temperature. Once convection occurs, the standard *Tiedtke* [1989] convection scheme is employed, though the buoyancy term includes the dependency on the variance of virtual potential temperature (refer to section 3.1).

### 3.3. Bulk Parameterization: Effects of Transient Shallow Cumulus

The ECHAM5_VSMF model includes a change to the representation of shallow convection made by *Isotta et al.* [2011]. Shallow convection, previously represented by the *Tiedtke* [1989] scheme, is replaced by the *Von Salzen and McFarlane* [2002] scheme. The *Von Salzen and McFarlane* [2002] shallow convection scheme is a bulk parameterization of an ensemble of transient shallow cumulus clouds, which accounts for two key processes: the life cycle of shallow cumulus clouds and inhomogeneities in the horizontal distribution of in-cloud properties. Both processes are greatly affected by the entrainment and detrainment rates, which differ over the lifetime of shallow cumulus cloud. In developing shallow cumulus clouds, inhomogeneities in cloud properties arise from the entrainment of environmental air in narrow regions near the top of rising cumulus cloud [*Kuo*, 1965]. When shallow cumulus clouds reach their maximum heights, rapid decay associated with lateral mixing occurs. This is approximated as an abrupt lateral detrainment of cloudy air into the environment [*Von Salzen and McFarlane*, 2002].

The shallow convection scheme in ECHAM5_VSMF begins by launching a test parcel from either the lowest three model levels or the surface, whichever has the highest moist static energy. The test parcel, representative of an ascending cloud, is lifted from the boundary layer through the level of free convection up to the level of neutral buoyancy. The ascent of the parcel is affected by entrainment and detrainment. If the pressure difference between the level of neutral buoyancy (LNB) and the level of free convection (LFC) is less than 300 hPa and if the ascent velocity is sufficiently strong to allow the test parcel to travel between two

vertical levels in a time step, shallow convection is permitted. Otherwise the clouds are classified as stratiform. The closure linking the cloud base mass flux with the convective vertical velocity scale, following *Grant* [2001], is based on a simplified turbulent kinetic energy (TKE) budget [*Isotta et al.*, 2011]. Should either of the following three conditions hold: (i) shallow convection does not trigger a cloud; or (ii) the level of neutral buoyancy is above the 0°C level; or (iii) the depth of the LNB-LFC exceeds 300 hPa; then the *Tiedtke* [1989] scheme is employed to determine if deep or midlevel convection exists [*Isotta et al.*, 2011]. The work of *Isotta et al.* [2011] found that the incorporation of the *Von Salzen and McFarlane* [2002] representation of shallow convection increased the low-level stratus and stratocumulus clouds because the frequency of shallow convection decreased and vertical mixing of moisture was reduced.

### 3.4. Dual Mass Flux

The time evolution of the large-scale equations for heat and moisture in ECHAM5 can be broken up into two parts: (i) the tendency due to turbulent mixing and convection and (ii) the tendency due to advection and diabatic processes. In ECHAM5_Std, the tendency due to turbulent mixing is parameterized in terms of eddy diffusivity, while convection is parameterized in terms of the convective mass flux [*Tiedtke*, 1989]. In the ECHAM5_DMF model version, the dual mass flux framework for boundary layer convection of *Neggers et al.* [2009] and *Neggers* [2009] is incorporated. Clouds and turbulent transport are represented as a function of the same bimodal joint distribution with a diffusive and an updraft component resulting in a internally consistent boundary layer scheme [*Neggers*, 2009]. The turbulent mixing parameterization includes both eddy diffusivity and an advective mass flux [*Neggers et al.*, 2009] (equation (1)). The eddy diffusivity term is parameterized as a function of turbulent kinetic energy [*Roeckner et al.*, 2003]. The advective mass flux represents organized updrafts [*Siebesma et al.*, 2007].

$$\overline{w'\phi'}_{turb} = A^{K}\overline{w'\phi'}^{K} + A^{up}\overline{w'\phi'}^{up} \tag{1}$$

In the Dual Mass Flux (DMF) equation (equation (1)), $w$ is the vertical velocity, $\phi$ can refer to both total specific humidity ($q_t$) and liquid water potential temperature ($\theta_l$). The superscript $K$ denotes the turbulent mixing due to eddy diffusion and $up$ denotes the turbulent mixing due to organized updrafts. $A^{up}$ is the area fraction covered by the organized updrafts (fixed at 10%) and the remainder $A^{K} = 1 - A^{up}$ is the area covered by eddy diffusion [*Neggers et al.*, 2009]. The advective mass flux (updrafts) is broken up into two parts: dry and moist updrafts (equation (2)).

$$\begin{aligned} A^{up}\overline{w'\phi'}^{up} &= M_{dry}(\phi_{dry} - \bar{\phi}) + M_{moist}(\phi_{moist} - \bar{\phi}) \\ &= a_{dry}w_{dry}(\phi_{dry} - \bar{\phi}) + a_{moist}w_{moist}(\phi_{moist} - \bar{\phi}) \end{aligned} \tag{2}$$

$(\phi - \bar{\phi})$ denotes the excess in $\phi$ of the dry and moist updraft over its environment [*Neggers et al.*, 2009]. The volumetric mass flux ($M$) for dry and moist updrafts is composed of the area fractions ($a$) covered by the dry and moist updrafts as well as vertical velocity ($w$). The partitioning of the bulk advective updraft amongst dry and moist updrafts allows for a smooth transition between the representation of different boundary layer clouds [*Neggers et al.*, 2009]. Areas with fractional cloud cover, such as those covered by shallow cumulus clouds, can be represented by some flexible ratio of $a_{moist}$ and $a_{dry}$. By changing the ratio of $a_{dry}$ and $a_{moist}$, different cloud regimes can be represented. For example, stratocumulus clouds would have $a_{moist} = 1$ and $a_{dry} = 0$, while the converse would be true for areas of solely dry convection. The $a_{moist}$ term is explicitly parameterized as a function of the proximity to saturation and the stability of the transition layer between turbulent mixed layer and convective cloud layer [*Neggers et al.*, 2009]. A $w_{dry,moist}$ is determined by vertically integrating a rising plume model [*Siebesma et al.*, 2007] from an initial state [*Neggers et al.*, 2009].

The ECHAM5_DMF also includes the formulation of vertical turbulent diffusion on conserved variables by *Siegenthaler-Le Drian* [2010]. Previously, turbulent diffusion in ECHAM5 was done on nonconserved variables, such as water vapor mixing ratio, liquid water mixing ratio, ice water mixing ratio, and dry static energy, which served to smooth the vertical profile of liquid water, destroying the cloud. *Siegenthaler-Le Drian* [2010] found that turbulent diffusion on conserved variables, specifically moist static energy and total
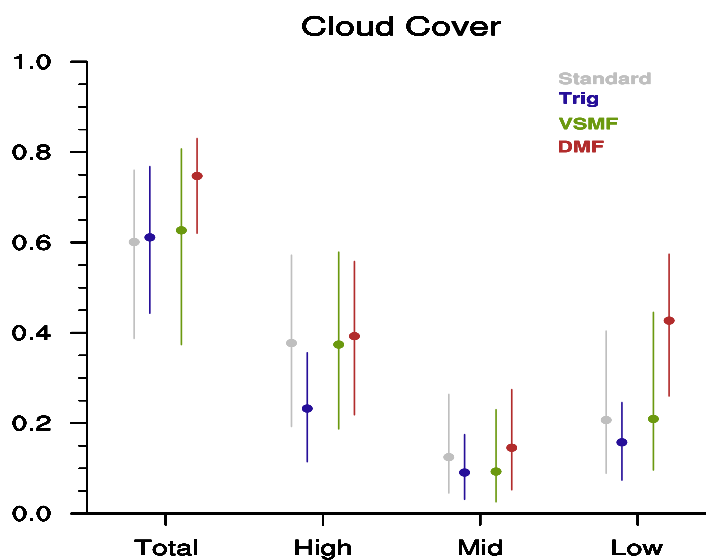
**Figure 1.** Total, high, mid, and low-level cloud cover in ECHAM5 for JJA 2007 from 45°N to 45°S. Median is represented by dots and bars indicate 25th and 75th percentiles.

water mixing ratio, by decreasing the minimal width of the total water mixing ratio PDF, increased the cloud cover.

In this experimental implementation of the ECHAM5_DMF scheme, cloud cover and cloud condensate in the boundary layer is modified. The modified clouds interact with the model's cloud microphysics and precipitation formation schemes. In the coupling to radiation in the following time step, cloud cover is updated by the default cloud scheme of the model which also diagnoses cloud cover and computes cloud condensate above the boundary layer. This experimental model version is not tuned to obtain a top-of-atmosphere radiation balance close to the observed one. As expected, cloud radiative effects are considerably perturbed due to the substantially altered cloud fraction.

## 4. Cloud Cover

This comparison focuses on the representation of clouds and precipitation by the three new boundary layer schemes. The comparison will be broken into three sections: (i) the purely modeled cloud cover; (ii) the cloud cover as determined by the lidar simulator; and (iii) the reflective properties of hydrometeors as determined by the radar simulator. The comparison of the three schemes will be initially made with the standard ECHAM5 model as it is vital to understand the differences amongst model versions before beginning the analysis with the satellite simulators. This will be followed by the comparison of the new schemes with the CALIPSO and CloudSat satellite retrievals.

Throughout the study, references of high, mid, and low-level clouds refer to those with the following cloud top pressures ($p_{top}$) or altitudes (z) above sea level: (i) high level, $p_{top} < \sim 440\,hPa$, $z > 7.2\,km$; (ii) midlevel, $\sim 680\,hPa < p_{top} \geq \sim 440\,hPa$, $3.5 < z < 7.2\,km$; and (iii) low-level, $p_{top} \geq \sim 680\,hPa$, $z < 3.5\,km$ [*Rossow and Schiffer*, 1999].

The comparison of the high, middle, and low-level cloud fractions will specifically focus on the regions from 45°N to 45°S, which *Nam and Quaas* [2012] found to be poorly represented in standard ECHAM5. This region is especially important as the sensitivity of marine boundary layer clouds to changing environmental conditions currently constitutes the main source of uncertainty in tropical cloud feedbacks within GCMs [*Vial et al.*, 2013].

The modeled cloud fraction of each scheme, along with those diagnosed by the lidar simulator, is presented in Figures 1–3. For clarity, the following analysis is divided into three parts: comparison of the high-level cloud fraction produced by the three new schemes and standard ECHAM5, followed by the mid and low-level clouds. Understanding the changes in low-level clouds requires an appreciation of the changes to high-level clouds when using an active satellite simulator.

### 4.1. High-Level Cloud Cover
Figure 1 shows ECHAM5_Trig having a significant decrease in cloud cover, while ECHAM5_VSMF appears neutral and ECHAM5_DMF shows a slight increase in the high-level cloud cover compared to ECHAM5_Std. In the case of ECHAM5_Trig, the new formulation of the convective trigger has led to a more stringent governance of buoyant parcels of air. Parcels previously satisfying the criteria for convection no longer succeed. This implies that only the strongest convective events spur convection and the frequency of convection
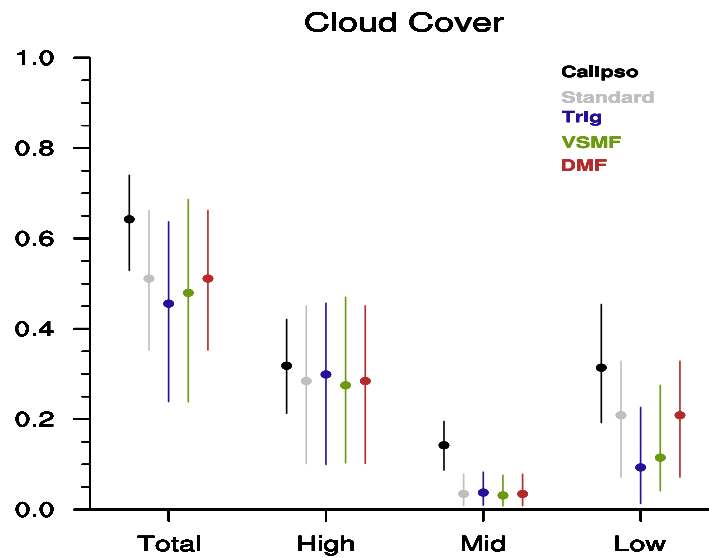
**Figure 2.** Total, high, mid, and low-level cloud cover from CALIPSO and ECHAM5 with the lidar simulator for JJA 2007 from 45°N to 45°S. Median is represented by dots and bars indicate 25th and 75th percentiles.

decreases. The decrease in ECHAM5_Trig purely modeled high-level cloud cover (Figure 1), however, is not reflected in the high-cloud cover determined by the lidar simulator (Figure 2). This is because the decrease in ECHAM5_Trig high-level clouds largely affected the SR bins <5 (not shown), which is below the common threshold that is used to define clouds by the lidar simulator. Any decrease in these clouds with a SR <5 would not be reflected in Figure 2 despite having a large affect on the pure model's 2-D projected cloud cover (Figures 1 and 3c).

ECHAM5_VSMF has a nearly identical tropical mean in high-level cloud cover compared to ECHAM5_Std, although it shows a wider distribution. Differences in their geographical distributions can be seen in Figure 3d. In *Isotta et al.* [2011], increases in ECHAM5_VSMF high-level tropical cloud cover, best seen in Figure 3d, was attributed to an increase in the frequency of midlevel convection at the expense of
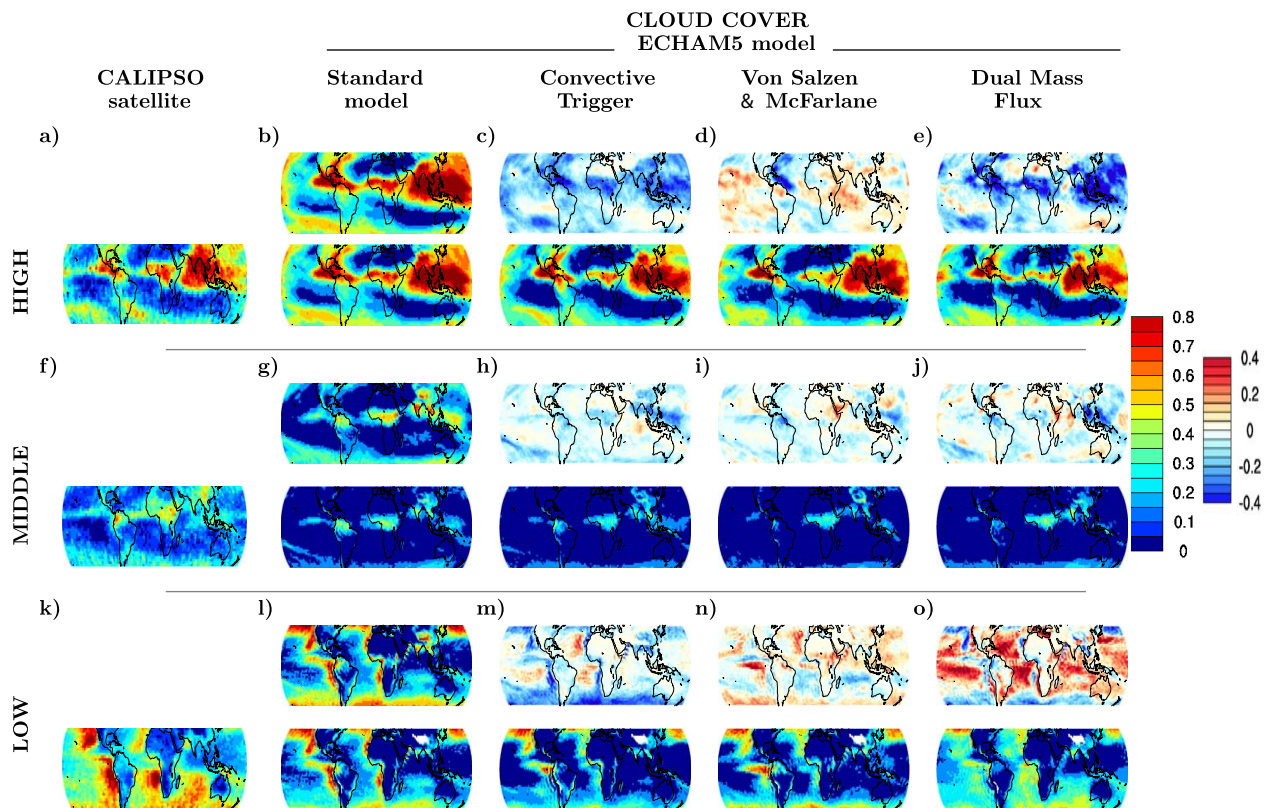


**Figure 3.** High-level clouds: (top row) high-level cloud cover for JJA 2007 from 45°N to 45°S in ECHAM5_Std as well as the differences of the three new boundary layer schemes to the standard model (e.g., Experiment-ECHAM5_Std). (bottom row) CALIPSO retrievals and all models with the lidar simulator. The midlevel and low-level cloud cover is similarly presented.

shallow convection in the Tropics. Since midlevel and deep convection is represented by the *Tiedtke* [1989] scheme, which is known to have small entrainment and detrainment rates, strong detrainment occurs at the cloud top accounting for the high-level Tropical clouds.

ECHAM5_DMF shows an overall increase in the high-level cloud cover (Figure 1). A closer look at Figure 3e show that the changes to the purely modeled high-level cloud distribution varies spatially. For example, there is a large increase in cloud cover over the Pacific Ocean and African continent. Conversely, there is a decrease in the cloud cover over the Indian continent and over the Intertropical Convergence Zone (ITCZ). The decrease in clouds over the ITCZ stems from greater vertical mixing throughout the atmospheric column in the ECHAM5_DMF compared to the *Tiedtke* [1989] scheme, and is therefore less likely to form convective anvils at the tropopause.

The lidar simulator diagnoses very similar distributions and amount of high-level cloud cover for the three new schemes (Figures 2 and 3a–3e), all of which agree well with CALIPSO retrievals. The models show a slight overestimate of cloud fraction within the ITCZ and an underestimate in the subsiding branches of the Hadley cell. All schemes have pronounced regional differences in high-level cloud cover compared to the ECHAM5_Std, varying up to ±20% locally (e.g. over Hawaii), however, the differences in high-level cloud cover are generally less than ±20% (absolute percent of cloud cover).

## 4.2. Midlevel Cloud Cover

Midlevel cloud cover of the three schemes shows very little change compared to ECHAM5_Std (Figures 1 and 3g–3j). The differences which do exist amongst the midlevel clouds of the schemes differ in both sign and region. For example, both the ECHAM5_Trig and ECHAM5_VSMF models generally show a decrease in cloud cover over the oceans, whereas the ECHAM5_DMF shows an increase of cloud cover over the continents. As previously discussed, the ECHAM5_Trig and ECHAM5_VSMF schemes suppress the frequency of occurrence of shallow convection, implying less transport of moisture to the midlevels. In the case of ECHAM5_DMF, more mixing throughout the atmosphere implies the cloud tops will be lower than previously determined, hence, slightly more midlevel clouds particularly over the land where convection is stronger.

The relatively small differences amongst the purely modeled midlevel clouds of the three schemes and ECHAM5_Std result in very little difference amongst the midlevel clouds diagnosed by the lidar simulator (Figures 2 and 3f–3j). Unfortunately, none of the new schemes improves the midlevel cloud cover and the midlevel cloud amounts remain vastly underestimated compared to the satellite retrievals.

## 4.3. Low-Level Cloud Cover

As expected, large differences between the three new schemes and the standard model are found in the low-level cloud cover. In ECHAM5_Trig, the convective trigger acts to suppress spurious convection, reducing ventilation of the boundary layer by shallow convection (Figures 3l–3o). This allows moisture to build up within the boundary layer, increasing the amount of oceanic low-level clouds particularly over regions typical of shallow convection. There is, however, a decrease in stratocumulus clouds causing the overall low-level cloud cover to decrease in the mean as well as the variability (Figure 1).

Unlike in ECHAM5_Trig, the changes in low-level cloud cover of ECHAM5_VSMF are not systematic. For example, not all cumulus regions show an increase in cloud cover, as in the southern Atlantic ocean and in the midlatitudes. *Isotta et al.* [2011] attributed decreases in low-level clouds to increased shallow convection which reduced the liquid water path and thereby cloud cover. Conversely, increases in low-level cloud cover were attributed to a reduction in vertical mixing of moisture resulting from a lower frequency of shallow convection activity [*Isotta et al.*, 2011]. Overall, there is a slight increase in low-level clouds as well as greater variability (Figure 1).

The ECHAM5_DMF shows the largest difference in cloud cover compared to ECHAM5_Std. Low-level cloud cover over the (Sub)Tropical oceans increases significantly; over 30% in many regions (e.g. Atlantic ocean). While an overall increase in cloud fraction of 20%–30% may appear extreme, bear in mind ECHAM5 had cloud fractions of less than 10% in many regions, which is well below values retrieved from satellites. The production of clouds in ECHAM5_DMF is the result of the different transport and cloud schemes employed. The ECHAM5_DMF can more readily affect the stability of the lower atmosphere via the changes to the transport schemes compared to the ones changing the shallow convection scheme alone. This in turn affects the skewness of the total water mixing ratio PDF. More or less clouds, depending on the PDF

skewness, with the same moisture in the boundary layer. As with the other two schemes, the ECHAM5_DMF shows a decrease in the stratocumulus cloud cover directly off the continents.

The low-level cloud cover derived by the lidar simulator, rather surprisingly, shows little difference amongst the ECHAM5_Std, ECHAM5_Trig and ECHAM5_VSMF maps (Figures 3k–3o). According to Figures 3m and 3n, both the ECHAM5_Trig and ECHAM5_VSMF have showed improvements in the (Sub)Tropical low-level cloud cover, including regional increases over 20%, yet not all changes in low-level cloud cover are captured by the lidar simulator. Take, for example, ECHAM5_Trig, focusing on the increase in trade cumulus clouds off the west coast of South America; a vast majority of the changes in cloud cover are not reflected in the lidar low-level cloud cover.

Further study of the lidar scattering ratios (not shown), from which one can determine where the lidar signal reaches full attenuation (SR $<$ 0.01), where there is clear sky (0.01 $<$ SR $<$1.2), where particles remain unclassified (1.2 $<$ SR $<$5) and where clouds occur (5 $<$ SR), showed that low-level clouds only yielded SR $>$ 60. In particular, SR $>$ 80 showed the most improvement in low-level cloud fraction though more so toward the midlatitudes and poles, suggesting that the low-level clouds modeled are optically bright. Interestingly, all three schemes were found to decrease (and improve) the frequency of lidar attenuation in terms of the zonal mean. The lidar attenuation, however, remains the greatest in the Tropics with fractions exceeding 0.5 at the surface in ECHAM5_Std and $\sim$0.3 in the other three schemes. Thus, the new schemes likely produce low-level clouds below high-level clouds which have already attenuated the lidar's signal, including in the subsiding branches of Hadley cell where high-level clouds are thought to be scarce. This latter aspect is likely to be particular to ECHAM5 which has already been shown to attenuate the lidar signal much higher in the atmosphere than observations, over regions of shallow cumulus and stratocumulus clouds, due to an overestimate of high-level clouds and an underestimation of effective ice crystal radius that exaggerates lidar scattering [*Nam and Quaas*, 2012]. As a result, ECHAM5_Trig and ECHAM5_VSMF appears to underestimate low-level cloud cover compared to CALIPSO retrievals. Future sensitivity studies regarding the exact threshold of cloud cover necessary for the lidar simulator to accurately detect clouds would be useful.

The lidar simulator, however, does show an improvement in low-level clouds for ECHAM5_DMF which best captures the low-level ocean clouds compared to CALIPSO retrievals. Despite the significant increase in low-level clouds, these clouds are still underestimated compared to CALIPSO, particularly in the stratocumulus regions. CALIPSO retrievals consistently show greater high, mid, low, and total-cloud cover than any of the models, but with less variability.

## 5. Radar Reflectivity Histograms

To better understand the differences in the representation of stratocumulus and shallow cumulus between the three boundary layer parameterization schemes, the joint histograms of cloud altitude and radar reflectivity histograms over the California Stratocumulus region (15° - 35°N; 110°W - 140°W) and Hawaiian Trade Cumulus (15°–35°N; 160°E–140°W) region will be evaluated (Figure 4). These two regions, as defined by *Webb et al.* [2001], have been shown to be better for the evaluation of low-level clouds with CloudSat observations and radar simulator compared to regimes of low-level clouds defined by large-scale environmental properties [*Nam and Quaas*, 2013]. The radar reflectivity histograms, commonly referred to as contoured frequency by altitude diagrams (CFADs), show the frequency of occurrence of clouds and precipitation from 0 to 19.2 km for intervals of radar reflectivities between $-27.5$ and 20 dBZe. The frequency of occurrence from CloudSat is normalized so each altitude sums to one, that is, the number of positive identifications in each reflectivity bin divided by the total number of measurements in that layer [*Bodas-Salcedo et al.*, 2008]. This can be compared to the frequency of occurrence determined from simulator output which gives the ratio of subcolumns with a given reflectivity to the total number of nonattenuated subcolumns for each grid box. Hydrometeors are identified as particles with radar reflectivities $> -27.5$ dBZe following *Bodas-Salcedo et al.* [2008] and *Marchand et al.* [2009].

The radar reflectivity histograms are very useful in evaluating the vertical distributions of clouds and precipitation. The radar reflectivity histograms can be roughly divided into four regions according to radar reflectivity and altitude of the hydrometeor. *Marchand et al.* [2009] state hydrometeors above 5 km are predominantly composed of ice whereas below 5 km they are predominantly liquid. In a sensitivity
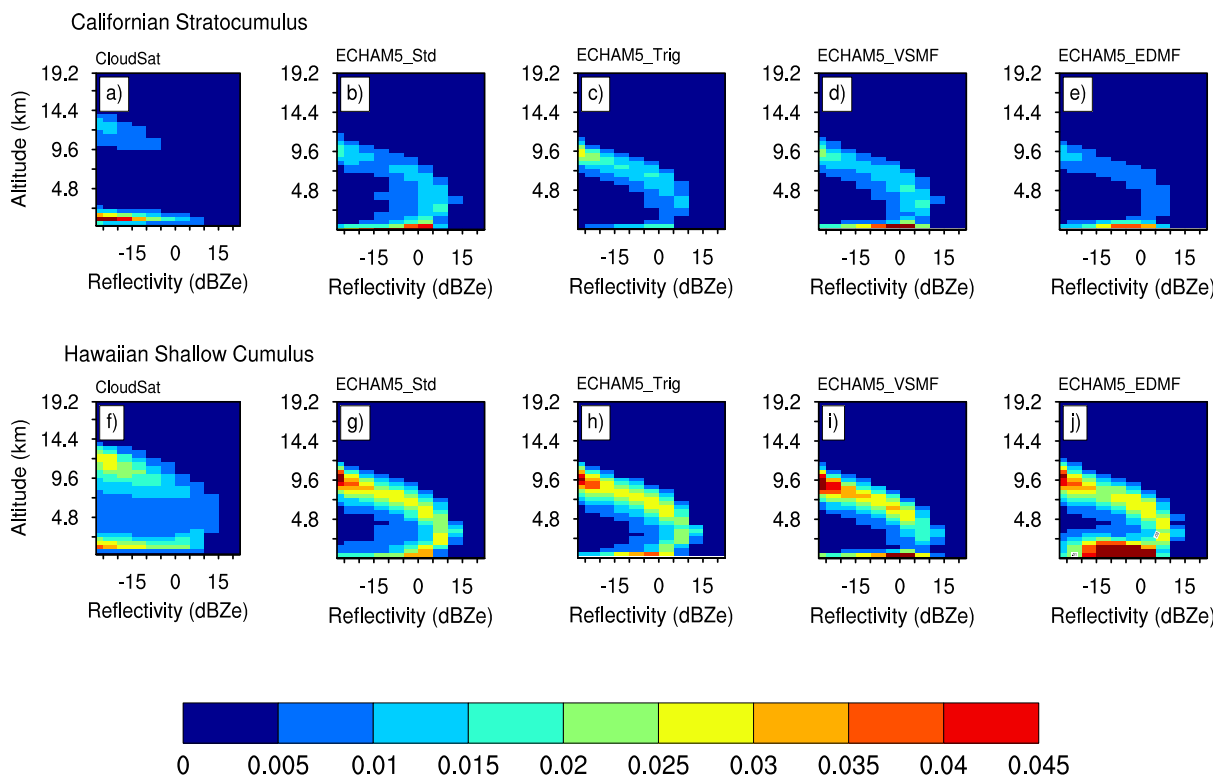
Figure 4. Cloud Altitude-Reflectivity Histogram for the Californian Stratocumulus and Hawaiian Trade Cumulus Cloud Regimes for JJA 2007.
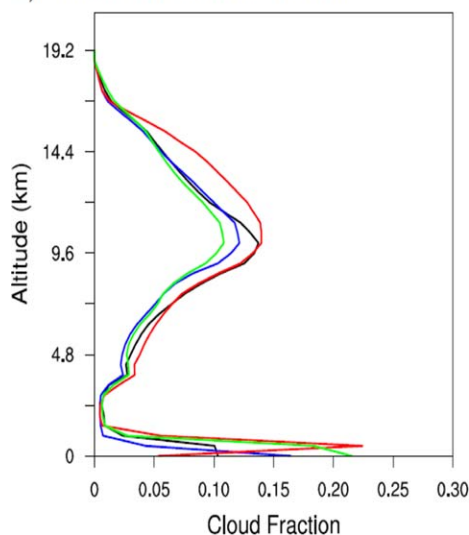
experiment, where precipitation is withheld from simulator for July 2007, *Nam and Quaas* [2013] found radar reflectivities $< -15$ dBZe in ECHAM5_Std are mainly nonprecipitating hydrometeors, whereas hydrometeors with $\geq -15$ dBZe were mainly precipitating over the California and Hawaii regions. Note that radar reflectivities below 1 km should be discarded due to ground clutter in the observations [*Tanelli et al.*, 2008; *Marchand et al.*, 2008]. Lastly, radar reflectivities are dominated by larger particles, and radar reflectivities will be in the precipitating region of the histogram in the presence of both precipitating and nonprecipitating hydrometeors.

### 5.1. Comparison to CloudSat

Despite the fact the lidar simulator did not show much difference amongst the cloud cover of ECHAM5_Std, ECHAM5_Trig, and ECHAM5_VSMF (Figure 1), the distribution of water in the atmospheric column is quite different (Figure 4). All schemes appear to overestimate the transport of moisture to the upper atmosphere and show a greater frequency of hydrometeors in the high-level and midlevels. Consequently, there is a significantly larger precipitation frequency originating at higher altitudes compared to the CloudSat satellite retrievals. In the boundary layer, all schemes show the greatest frequency of occurence in the precipitating half of the histogram ($\geq -15$ dBZe). None of the schemes are able to capture the peak in the nonprecipitating boundary layer quadrant which is found in the satellite retrievals. Over the Hawaiian region, the ECHAM5_DMF produces a realistic boundary layer depth, as reflected by radar reflectivities in the nonprecipitating quadrant (Figure 4j) compared to the ECHAM5_Std, ECHAM5_Trig, and ECHAM5_VSMF, all which have too shallow a boundary layer. In addition, the ECHAM5_DMF model has made the greatest stride toward reproducing the reflectivity distributions found from CloudSat shifting the peak frequency of occurrence toward lower reflectivities in the boundary layer. Since precipitation dominates the radar signal a closer look at the partitioning of convective and large-scale precipitation between the schemes is done in the next section.
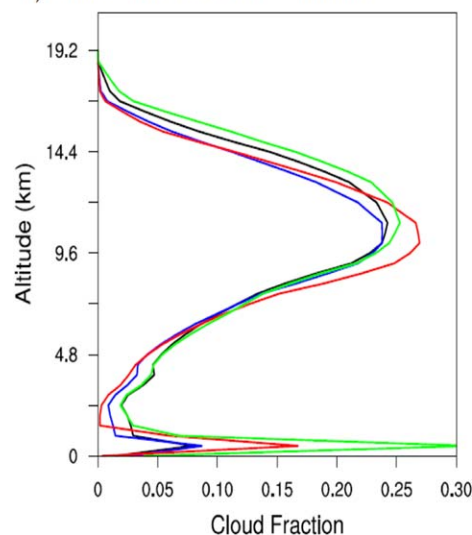
**Figure 5.** Regional cloud fraction profiles as determined purely by the model for JJA 2007: ECHAM5_Std (black); ECHAM5_Trig (Blue); ECHAM5_VSMF(Red); and ECHAM5_DMF(Green).

Though all schemes show different distributions of radar reflectivities, the differences amongst the schemes are less than their respective differences to the CloudSat retrievals.

### 5.2. Comparison to ECHAM5_Std

Comparison of the Californian stratocumulus histograms, Figures 4b and 4c, show ECHAM5_Trig having an increased frequency of occurrence of high-level nonprecipitating ice clouds compared to ECHAM5_Std. Deep-level and midlevel convection are still parameterized by the *Nordeng* [1994] and *Tiedtke* [1989], and the *Tiedtke* [1989] scheme, respectively, in all the models. The *Tiedtke* [1989] scheme is known for overestimating the mass flux and as such the frequency of high-level clouds is overestimated according to the radar joint cloud altitude-reflectivity histogram. In ECHAM5_Trig there is an increased transport of moisture to the upper atmosphere which is caused by convective events stemming from a moister boundary layer. The additional moisture brought into the upper atmosphere increases the likelihood of precipitation at high altitudes as seen in the radar reflectivity histogram ($>-15$ dBZe). Over the Californian region, ECHAM5_Trig shows a greater frequency of precipitation ($>-15$ dBZe) at high and midlevels compared to the ECHAM5_Std model. This is not as evident over the Hawaiian region. It should be noted that in the lowest level, frequency of precipitation with reflectivities $>0$ dBZe decreased, however, the likelihood of detecting low-level nonprecipitating clouds with the radar simulator did not increase.

In fact, fewer low-level clouds in the nonprecipitating part of the histogram are detected in ECHAM5_Trig than ECHAM5_Std even though more low-level clouds modeled in each region (Figure 5). It is likely, the abundance of higher-lying clouds and precipitating hydrometeors obscured the reflectivities from the low-clouds [*Nam and Quaas*, 2012], particularly since the low-level clouds produced purely by the models rarely develop above 1 km. It is possible, though less likely, that the radar simulator does not detect the newly formed clouds because of a slight underestimate in the effective radius of cloud liquid water as in ECHAM5_Std [*Nam and Quaas*, 2012]. As with ECHAM5_Trig, the ECHAM5_VSMF shows a greater frequency of high-level ice clouds and precipitation compared to ECHAM5_Std in the Californian stratocumulus and Hawaiian shallow cumulus regions (Figures 4d and 4h). In these plots, the increased frequency of midlevel precipitating hydrometeors are consistent with the increased the frequency of midlevel convection in the Tropics which was found by *Isotta et al.* [2011]. The increase in convection events provides both more moisture to the upper atmosphere for precipitation in addition to larger particles and higher reflectivities. In regards to the lowest layers of the atmosphere, the ECHAM5_VSMF shows a significant increase in precipitation frequency, which is due to the incorporation of the life cycle of shallow cumulus clouds. Abrupt

detrainment at the end of the shallow cumulus life cycle provides large amounts of moisture for precipitation in the low-levels of the atmosphere. This is also likely the cause of a break in the precipitation reflectivities around 2 km. Despite the increase in frequency of precipitation, ECHAM5_VSMF also shows an increase in the frequency nonprecipitating boundary layer clouds in the Californian stratocumulus region. The same holds true for the Hawaiian shallow cumulus region.

The ECHAM5_DMF, unlike the previous two schemes, shows a decrease in the frequency of high-level clouds and precipitation. In the Californian stratocumulus region, the development of nonprecipitating boundary layer clouds is not evident as the peak in reflectivities remains in the precipitating half of the histogram, obscuring the clouds. There is, however, a slight shift toward lower radar reflectivities. In the Hawaiian shallow cumulus region, the most prominent feature is the increase of low-reflectivity hydrometeors in the lowest levels, particularly in the nonprecipitating region of the histogram. This is due to the advective component of the double PDF which represents cumuliform clouds in conditionally unstable layers. Though the ECHAM5_DMF strongly overestimates the frequency of precipitation at the lowest levels, it is the scheme which best succeeds at substantially increasing the frequency of nonprecipitating boundary layer clouds.

## 6. Changes in Precipitation

ECHAM5_Std has been found to capture the zonal and global distribution pattern of accumulated surface precipitation well compared to observations [*Hagemann et al.*, 2006], however, as with many GCMs it underestimates the contribution and frequency of heavy ($>20$ mm d$^{-1}$) precipitation and overestimate light ($<10$ mm d$^{-1}$) precipitation [*Dai*, 2006]. In order to understand the differences found in radar reflectivity histograms, we first consider the influence of precipitation intensity on the radar reflectivity histogram on ECHAM5_Std, and afterward we consider the differences in large-scale and convective precipitation between the three schemes compared to ECHAM5_Std.

Using ECHAM5_Std, a series of short sensitivity experiments of 1 day (latitude $\times$ longitude $\times$ 3 h time steps $= 192 \times 96 \times 8 = 147,456$ grid boxes) where precipitation exceeding various intensities were withheld from the COSP simulator. In the first experiment, all large-scale and convective precipitating rain with intensities exceeding 0.01 mm d$^{-1}$, as well as all precipitating snow, were withheld from the simulator. In a sequential manner, precipitating rain with intensities $> 0.1, > 1$, and $> 10$ mm d$^{-1}$ were withheld. Precipitating rain with intensities $< 0.01$ mm d$^{-1}$ yielded radar reflectivities $>15$ dBZe and rather surprisingly, all other experiments yielded identical radar reflectivity histograms as the $<0.01$ mm d$^{-1}$ experiment (not shown). This implies that large-scale precipitation of $<0.01$ mm d$^{-1}$ is the dominating contributor to the radar reflectivity histograms and greatest source of differences between the model and CloudSat observations. Any scheme which reduces the frequency of precipitation intensities $<0.01$ mm d$^{-1}$ would improve the radar reflectivity histogram. As a final sensitivity experiment, all large-scale precipitation was withheld from the simulator to determine the contribution of convective precipitation. It was found that convective rain plays an inconsequential role in the ECHAM5_Std radar reflectivity histogram.

A closer study of the division of precipitation is presented for the region of Hawaii for varying precipitation intensities. The greatest frequency of precipitative events in ECHAM5_Std are from large-scale low-intensity events (Figure 6). The convective events occur more frequently at much greater intensities. Compared to the global model, the Hawaii region of ECHAM5_Std has higher frequencies of the lowest intensity precipitation events (not shown).

Of the three new parameterization schemes, the changes in the ECHAM5_Trig precipitation frequency are the smallest (i.e., less than 0.25). The large-scale precipitative events show a decrease in the lowest intensity events and an increase in the midrange events. Similarly, convective events show a decrease in the frequency of occurrence in the lowest intensity events and an increase in the highest intensity events. This most likely caused by the diminution of shallow convection which implies that only the strongest convective events are allowed to develop. This in turn transports moisture more effectively to higher altitudes, acting as an input to the large-scale moisture budget and thus increasing the intensity large-scale precipitation.

The greatest changes in precipitation occur in the ECHAM5_VSMF scheme. *Isotta et al.* [2011] states ECHAM5_VSMF does not change the amount of surface precipitation at the global scale even though a
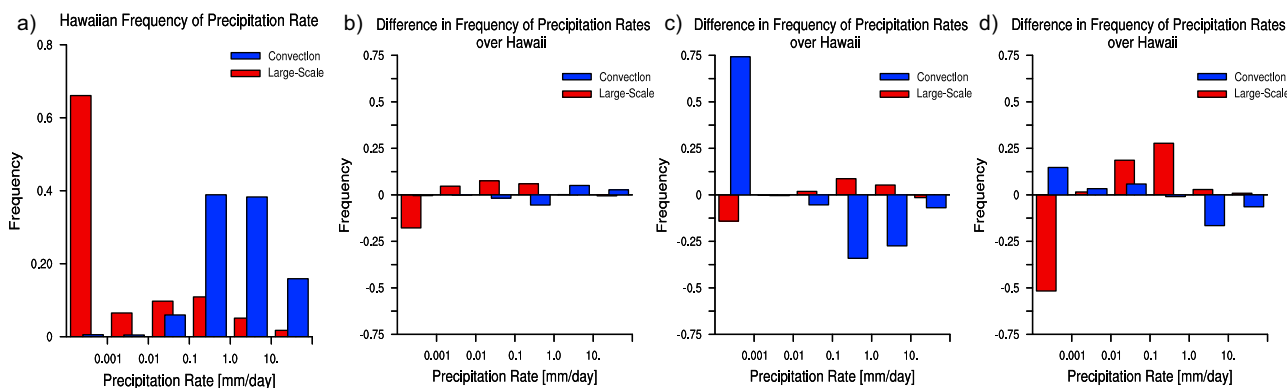
**Figure 6.** Frequency of occurrence of large-scale and convective precipitation events of varying intensities over Hawaii (JJA 2007). (a) ECHAM5_Std. Difference between (b) ECHAM5_Trig, (c) ECHAM5_VSMF, and (d) ECHAM5_DMF and ECHAM5_Std.

significant change in the partitioning of large-scale and convective precipitation was found. Focusing on the convective precipitative events, there is a significant increase in the frequency of precipitation in the lowest intensity precipitation bin. This is because shallow convection contributes to convective precipitation, unlike the ECHAM5_Std. Its contribution to the total precipitation, however, is very small. Conversely, high-intensity convective precipitation events decrease significantly. Both of which are likely due to the inclusion of the life cycle of shallow cumulus and detrainment of moisture. The large-scale precipitation shows a decrease of the lowest intensity events and an increase in the midintensity events. The changes to the large-scale precipitation events are likely due to the abrupt detrainment of moisture into the atmosphere at the end of the shallow cumulus life cycle.

The ECHAM5_DMF shows the greatest change in large-scale precipitation. As in the other two schemes, but to a larger extent, there is a decrease in the frequency of precipitation in the lowest intensity bin and an increase in the midlevel intensity bin of large-scale precipitation. The convective precipitation shows a distribution of changes, with an increase in the lower intensity events and a decrease in the highest intensity events. This is likely due to the increase in low-level cloud amount which increases the likelihood of higher-intensity precipitation.

In summary, all three schemes show a decrease in the frequency of the low-intensity bin of large-scale precipitation and increase in the midintensity precipitation. In regards to the convective precipitation, there are no systematic changes in the distribution of precipitation intensities. Despite the fact that the radar simulator shows an overestimation of precipitating hydrometeors in the histograms, the three new schemes all show an improvement in the distribution of precipitation at the surface.

## 7. Conclusions and Discussion

*Nam and Quaas* [2012] showed that ECHAM5 GCM underestimates low-level clouds; particularly in the (Sub)Tropics, in comparison to CALIPSO satellite retrievals motivating the study of different representations of boundary layer clouds. As such, three new representations of boundary layer clouds aiming to improve the representation of (Sub)Tropical clouds in ECHAM5 were compared with CALIPSO and CloudSat satellite retrievals. Along with the standard ECHAM5 model, a modified version of the *Tiedtke* [1989] scheme (ECHAM5_Trig), a bulk parameterization of transient shallow cumulus clouds (ECHAM5_VSMF), and a dual mass flux scheme (ECHAM5_DMF) were incorporated and evaluated.

A comparison of the purely modeled cloud maps with ECHAM5_Std showed that the three new schemes improved the low-level cloud cover, particularly over the oceans. Much of the changes to the low-level cloud cover in the ECHAM5_Trig and ECHAM5_VSMF models, however, were not captured by the lidar simulator. This is because the new schemes likely produce low-level clouds below high-level clouds which have already attenuated the lidar's signal, including in the subsiding branches of Hadley cell where high-level clouds are thought to be rare. High-level clouds in ECHAM5 have been found to overestimate compared to observations and attenuate the lidar signal much higher in the atmosphere than observations due to an

underestimation of effective ice crystal radius that exaggerates lidar scattering [*Nam and Quaas*, 2012]. In the case of ECHAM5_DMF, there was a significant increase in low-level cloud cover which the lidar simulator captured for the most part. Despite of having the greatest amount of low-level clouds, however, even the ECHAM5_DMF underestimates the low-level cloud cover compared to the retrievals.

A further study of the Californian and Hawaiian regions was made to better understand the representation of stratocumulus and shallow cumulus clouds regimes. Compared to CloudSat, the three schemes overestimate the frequency of high-level clouds, as well as overestimate the frequency of precipitation originating at high levels, similar to ECHAM5_Std as concluded in *Nam and Quaas* [2012]. A series of short sensitivity experiments indicate that large-scale precipitation intensities of $<0.01$ mm d$^{-1}$ are the dominating contributor to the radar reflectivity histograms and are the largest source differences between ECHAM5 and CloudSat radar reflectivity histograms. The overly frequent precipitating hydrometeors are likely to have obscured the reflectivities from the low-clouds [*Nam and Quaas*, 2013]. In ECHAM5_Trig and ECHAM5_VSMF, the increase in low-level cloud cover also increased frequency of high-level clouds over the Californian and Hawaiian regions. This is likely because convection stemming from a moister boundary layer transports more moisture to the higher altitudes. Since deep-level and midlevel convection are still parameterized by the *Tiedtke* [1989] and *Nordeng* [1994], and *Tiedtke* [1989] scheme, respectively, which is known for overestimating the mass flux, it is not surprising that the frequency of high-level clouds is overestimated according to the radar joint cloud altitude-reflectivity histogram.

The overestimation of precipitation frequency in each scheme stems from different causes. The partitioning between large-scale and convective precipitation for various intensities differs for the four schemes. All the schemes show an improvement by decreasing low-intensity large-scale precipitation and increase in higher-intensity precipitation. There is, however, no systematic change in the convective precipitation.

Lastly, the low-level clouds produced purely in the Californian stratocumulus and Hawaiian shallow cumulus regions by the new schemes are around 1 km and generally do not develop at higher altitudes. The ECHAM5_DMF, with its modified transport scheme, shows the most promise in producing a more realistic boundary layer depth as indicated by the frequency of reflectivities in the nonprecipitating quadrant of the radar reflectivity histogram. The implementation of this cloud scheme, however, remains experimental and it is important to note that the top-of-atmosphere radiation balance has not been tuned to obtain observed distributions.

The differences amongst the schemes, however, are less than those compared to the satellite retrievals.

Looking forward, as computational speed and efficiency increases, climate models will run at much higher resolutions and one must consider the impact of finer discretizations on existing subgrid parameterization schemes. In addition to the general improvement of the mean atmospheric state, which accompanies an increase in horizontal resolution, the parameterization schemes would benefit from localized atmospheric profiles. An increase in vertical resolution, particularly in the boundary layer, would allow for a more accurate representation of parcel ascent; which is essential for convective processes. In the case of ECHAM5_VSMF, for example, increasing the number of starting layers of the test parcel would allow for a more precise representation of shallow convection. In addition, there is current research focusing on the reformulation of the ECHAM5_DMF scheme to make it scale aware and scale adaptive. The reformulation depends on resolving the probability density function of an ensemble of clouds as a function of size (l) and height (z) using a rising plume model, thereby allowing the bulk plume model to be aware of the underlying range of scales of the processes it represents *Neggers* [2013].

## References

Bodas-Salcedo, A., M. J. Webb, M. E. Brooks, M. A. Ringer, K. D. William, S. F. Milton, and D. R. Wilson (2008), Evaluating cloud systems in the Met Office global forecast model using simulated CloudSat radar reflectivities, *J. Geophys. Res., 113*, D00A13, doi:10.1029/2007JD009620.

Bodas-Salcedo, A., et al. (2011), COSP: Satellite simulation software for model assessment, *Bull. Am. Meteorol. Soc., 92*, 1023–1043, doi:10.1175/2011BAMS2856.1.

Bony, S., and J. Dufresne (2005), Marine boundary layer clouds at the heart of tropical cloud feedback uncertainties in climate models, *Geophys. Res. Lett., 32*, L20806, doi:10.1029/2005GL023851.

Cess, R., et al. (1990), Intercomparison and interpretation of climate feedback processes in 19 atmospheric general circulation models, *J. Geophys. Res., 95*, 16,601–16,615, doi:10.1029/JD095iD10p16601.

Chepfer, H., S. Bony, D. Winker, M. Chiriaco, J. Dufresne, and G. Sèze (2008), Use of CALIPSO lidar observations to evaluate the cloudiness simulated by a climate model, *Geophys. Res. Lett.*, *35*, L15704, doi:10.1029/2008GL034207.

Chepfer, H., S. Bony, D. Winker, G. Cesana, J. Dufresne, P. Minnis, C. Stubenrauch, and S. Zeng (2010), The GCM oriented calipso cloud product (CALIPSO-GOCCP), *J. Geophys. Res.*, *115*, D00H16, doi:10.1029/2009JD012251.

Dai, A. (2006), Precipitation characteristics in eighteen coupled climate models, *J. Clim.*, *19*, 4605–4630.

Grant, A. (2001), Cloud-base fluxes in the cumulus-capped boundary layer, *Q. J. R. Meteorol. Soc.*, *127*, 407–421.

Hagemann, S., K. Arpe, and E. Roeckner (2006), Evaluation of the hydrological cycle in the ECHAM5 model, *J. Clim.*, *19*, 3810–3827.

Haynes, J., R. Marchand, Z. Luo, A. Bodas-Salcedo, and G. Stephens (2007), A multipurpose radar simulation package: Quickbeam, *Bull. Am. Meteorol. Soc.*, *88*, 1723–1727.

Isotta, F. A., P. Spichtinger, U. Lohmann, and K. von Salzen (2011), Improvement and implementation of a parameterization for shallow cumulus in the global climate model ECHAM5-HAM, *J. Atmos. Sci.*, *68*, 515–532, doi:10.1175/2010JAS3447.1.

Karlsson, J., G. Svensson, and H. Rodhe (2008), Cloud radiative forcing of subtropical low level clouds in global models, *Clim. Dyn.*, *30*, 779–788, doi:10.1007/s00382-007-0322-1.

Klein, S., and C. Jakob (1999), Validation and sensitivities of frontal clouds simulated by the ECMWF model, *Mon. Weather Rev.*, *127*, 2514–2531.

Kuo, H. L. (1965), On formation and intensification of tropical cyclones through latent heat release by cumulus convection, *J. Atmos. Sci.*, *22*, 40–63.

Lin, S. J., and R. B. Rood (1996), Multidimensional ux form semi-lagrangian transport, *Mon. Weather Rev.*, *124*, 2046–2068.

Lohmann, U., and E. Roeckner (1996), Design and performance of a new cloud microphysics scheme developed for the echam4 general circulation model, *Clim. Dyn.*, *12*, 557–572.

Mace, G., R. Marchand, Q. Zhang, and G. Stephens (2007), Global hydrometeor occurrence as observed by CloudSat; initial observations from summer 2006, *Geophys. Res. Lett.*, *34*, L09808, doi:10.1029/2006GL029017.

Marchand, R., G. Mace, T. Ackerman, and G. Stephens (2008), Hydrometeor detection using CloudSat—An earth-orbiting 94-ghz cloud radar, *J. Atmos. Oceanic Technol.*, *25*, 519–533.

Marchand, R., J. Haynes, G. Mace, T. Ackerman, and G. Stephens (2009), A comparison of simulated cloud radar output from the multiscale modeling framework global climate model with CloudSat cloud radar observations, *J. Geophys. Res.*, *114*, D00A20, doi:10.1029/2008JD009790.

Moebis, B., and B. Stevens (2012), Factors controlling the position of the Intertropical Convergence Zone on an aquaplanet, *J. Adv. Model. Earth Syst.*, *4*, M00A04, doi:10.1029/2012MS000199.

Nam, C., and J. Quaas (2012), Evaluation of clouds and precipitation in the ECHAM5 general circulation model using CALIPSO and CloudSat satellite data, *J. Clim.*, *25*, 4975–4992, doi:10.1175/JCLI-D-11-00347.1.

Nam, C., and J. Quaas (2013), Geographically versus dynamically defined boundary layer cloud regimes and their use to evaluate general circulation model cloud parameterizations, *Geophys. Res. Lett.*, *40*, 4951–4956, doi:10.1002/grl.50945.

Neggers, R. (2009), A dual mass flux framework for boundary layer convection. Part II: Clouds, *J. Atmos. Sci.*, *66*, 1489–1506.

Neggers, R. (2013), Humidity-convection feedbacks in a mass flux scheme based on resolved size densities, paper presented at the ECMWF Workshop on the Parameterization of Clouds and Precipitation Across Scales, Reading, 5–8 Nov., European Center for Medium-Range Weather Forecast (ECMWF), Reading, U. K.

Neggers, R., M. Koehler, and A. Beljaars (2009), A dual mass flux framework for boundary layer convection. Part I: Transport, *J. Atmos. Sci.*, *66*, 1465–1487.

Nordeng, T. (1994), Extended versions of the convective parameterization scheme at ECMWF and their impact on the mean and transient activity of the model in the Tropics, *Tech. Rep. 206*, 41 pp., European Center for Medium-Range Weather Forecast (ECMWF), Reading, U. K.

Ringer, M., et al. (2006), Global mean cloud feedbacks in idealized climate change experiments, *Geophys. Res. Lett.*, *33*, L07718, doi:10.1029/2005GL025370.

Roeckner, E., et al. (2003), The Atmospheric General Circulation Model ECHAM5: Part 1, Tech. Rep. 349, Max Planck Inst. for Meteorol., Hamburg, Germany.

Rossow, W., and R. Schiffer (1999), Advances in understanding clouds from ISCCP, *Bull. Am. Meteorol. Soc.*, *80*, 2261–2287.

Siebesma, A., and J. Cuijpers (1995), Evaluation of parametric assumptions for shallow cumulus convection, *J. Atmos. Sci.*, *52*, 650–666.

Siebesma, A., et al. (2003), A large eddy simulation intercomparison study of shallow cumulus convection, *J. Atmos. Sci.*, *60*, 1201–1219.

Siebesma, A., P. Soares, and J. Teixeira (2007), A combined eddy-diffusivity mass-flux approach for the convective boundary layer, *J. Atmos. Sci.*, *64*, 1230–1248.

Siegenthaler-Le Drian, C. (2010), *Stratocumulus clouds in ECHAM5-HAM*, PhD thesis, Swiss Federal Inst. of Technol. (ETHZ), Zurich, Switzerland, doi:10.3929/ethz-a-006073454.

Soden, B., and I. Held (2006), An assessment of climate feedbacks in coupled oceanatmosphere models, *J. Clim.*, *19*, 3354–3360, doi:10.1175/JCLI3799.1.

Stevens, B., et al. (2013), Atmospheric component of the MPI-M Earth System Model: ECHAM6, *J. Adv. Model. Earth Syst.*, *5*, 146–172, doi:10.1002/jame.20015.

Svensson, G., M. Tjernstroem, and D. Koracin (2000), The sensitivity of a stratocumulus transition: Model simulations of the astex first lagrangian, *Boundary Layer Meteorol.*, *95*, 57–90.

Tanelli, S., S. Durden, E. Im, K. Pak, D. Reinke, P. Partain, R. Marchand, and J. Haynes (2008), CloudSats cloud profiling radar after 2 years in orbit: Performance, external calibration, and processing, *IEEE Trans. Geosci. Remote Sens.*, *46*(11), 3560–3573.

Tiedtke, M. (1989), A comprehensive mass flux scheme for cumulus parameterization in large-scale models, *Mon. Weather Rev.*, *117*, 1779–1800.

Tompkins, A. M. (2002), A prognostic parameterization for the subgrid-scale variability of water vapor and clouds in large-scale models and its use to diagnose cloud cover, *J. Atmos. Sci.*, *59*, 1917–1942.

Vial, J., S. Bony, and J.-L. Dufresne (2013), On the interpretation of inter-model spread in CMIP5 climate sensitivity estimates, *Clim. Dyn.*, *41*, 3339–3362, doi:10.1007/s00382-013-1725-9.

Von Salzen, K., and N. McFarlane (2002), Parameterization of the bulk effects of lateral and cloud-top entrainment in transient shallow cumulus clouds, *J. Atmos. Sci.*, *59*, 1405–1430.

Wang, Y., L. Zhou, and K. Hamilton (2007), Effect of convective entrainment/detrainment on the simulation of the tropical precipitation diurnal cycle, *Mon. Weather Rev.*, *135*, 567–585.

Webb, M., C. Senior, S. Bony, and J.-J. Morcrette (2001), Combining ERBE and ISCCP data to assess clouds in the Hadley Centre, ECMWF and LMD atmospheric climate models, *Clim. Dyn.*, *17*(12), 905–922.

Winker, D. M., W. Hunt, and M. McGill (2007), Initial performance assessment of CALIOP, *Geophys. Res. Lett.*, *34*, L19803, doi:10.1029/2007GL030135.